

Bidirectional Evolutionary Stress-Based Topology Optimization: Global P-Measure Approach for the von Mises-Hencky and Drucker-Prager Failure Criteria

João Gonçalves Lima Neto^{a*} , Renato Pavanello^b

Department of Computational Mechanics, Faculty of Mechanical Engineering, University of Campinas, Campinas, Brazil ^aj246078@dac.unicamp.br; ^bpava@fem.unicamp.br

* Corresponding author

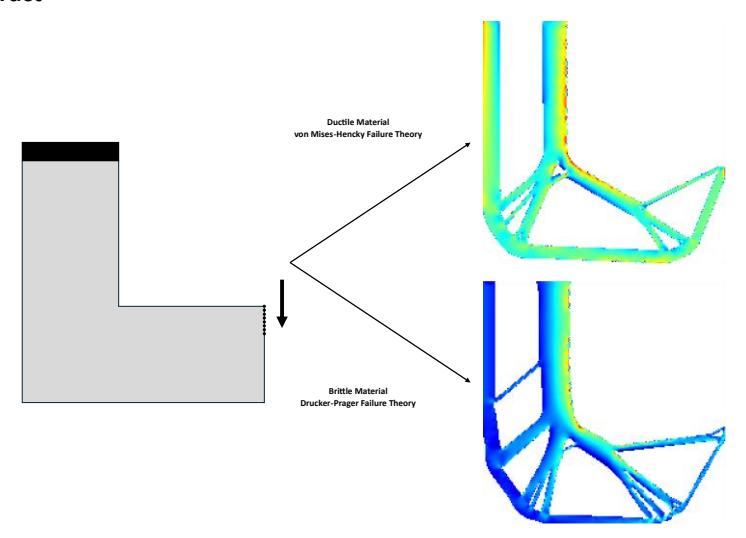
Abstract

This work presents a methodology for stress-based topology optimization using the bidirectional evolutionary structural optimization method, considering static failure theories. The base problem is formulated in a general form as the maximization of the P-measure — an aggregation function derived from the P-norm — of the safety factor associated with an arbitrary static failure criterion, under a volume constraint. The formulation is examined for von Mises-Hencky and Drucker-Prager static failure theories, allowing the proposed approach to be applied to a wide range of ductile and brittle materials. Through selected numerical examples, it is demonstrated that the method successfully produces topologies with maximum stress magnitudes consistent with reference results for the von Mises-Hencky criterion. Moreover, it achieves topologies with reduced stress concentration and higher safety factors compared to the traditional mean-compliance-based approach when using the Drucker-Prager failure criterion.

Keywords

Bidirectional evolutionary structural optimization, stress-based topology optimization, static failure criteria

Graphical Abstract



1 INTRODUCTION

In recent years, topology optimization has evolved from a theoretical concept into a key technology for high-performance lightweight design. By automatically redistributing material within a given domain, it enables the creation of structurally efficient and functionally optimized components, particularly relevant to additive manufacturing and multimaterial design. Among the existing strategies, evolutionary approaches, such as the Bidirectional Evolutionary Structural Optimization (BESO) method, stand out for their simplicity, robustness, and clear physical interpretation (Huang and Xie, 2007). These methods iteratively evolve the structural layout by adding or removing material based on sensitivity information, simulating a process of natural selection toward optimal performance.

While early BESO formulations were primarily developed for compliance minimization, recent studies have pushed the method toward more realistic design criteria, especially those driven by stress and failure considerations. In stress-based topology optimization, the objective typically involves minimizing a stress measure or maximizing a safety factor under a volume constraint. This approach directly addresses the key limitation of compliance-based designs, namely, the uncontrolled stress concentrations that often arise in the final layouts.

Significant advances have been achieved in this direction. The global P-norm aggregation of von Mises stresses (Xia et al., 2018) provided a mathematically consistent way to handle local stress constraints within the BESO framework. Later developments introduced local stress limits at the element level (Zhao et al., 2019), geometric (Xu, Han and Zhao, 2020) and material (Han et al., 2021; Xu, Han and Zhao, 2021) nonlinearities, and relaxation strategies for improved convergence (Ma et al., 2021). Stress-based BESO methods have also been extended to design-dependent loads (Garcez, 2021), multi-material structures (Han, 2024), and transient loading regimes (Li et al., 2024). These developments collectively illustrate the growing maturity and versatility of BESO for high-fidelity structural design.

Despite these advances, most stress-based formulations remain anchored to the von Mises-Hencky criterion, which assumes ductile behavior and isotropic yielding (Dowling, 2013). Modern applications of topology optimization increasingly demand structural design across a wide range of materials, including ceramics, concrete, and brittle polymers, where failure mechanisms deviate significantly from the von Mises hypothesis. Extending stress-based topology optimization beyond this limitation is therefore essential for achieving failure-aware designs suitable for brittle materials. Significant contributions have been made in this regard by Jeong et al. (2012), Giraldo-Londoño and Paulino (2020), and Kundu, Li, and Zhang (2022), who proposed formulations capable of capturing the distinct failure mechanisms within the topology optimization framework.

Another limitation in existing studies concerns the definition of the stress-based objective function or constraint itself. Many works directly address equivalent stress measures, which do not always provide a consistent representation of structural safety across different failure theories. In fact, an equivalent stress measure is well-defined only for the von Mises-Hencky theory, which assumes isotropic yielding. For most other static failure theories, particularly those intended for brittle or pressure-sensitive materials, failure cannot be described by a single scalar equivalent stress, since the envelope depends not only on the stress magnitude but also on its orientation, principal stress combination, and hydrostatic sensitivity (Dowling, 2013). Based on this, most studies employing alternative failure theories formulate their methodologies directly in terms of the yield or failure function, rather than through an equivalent stress measure. This is the case in the works of Luo and Kang (2012), Giraldo-Londoño and Paulino (2020) — who proposed a unified yield function applicable to multiple failure criteria —, Kundu, Li, and Zhang (2022), among others. Such formulations allow for capturing complex failure envelopes but often lack a direct and intuitive link to the concept of structural safety.

However, expressing the optimization problem in terms of the safety factor can be more advantageous. This approach provides a unified and physically interpretable metric that inherently accounts for the geometry of the failure envelope, regardless of its shape or symmetry. Furthermore, a safety-factor-based formulation naturally aligns with engineering design practice, facilitates comparison across different materials, and can be straightforwardly extended to other failure mechanisms, such as fatigue. This perspective has been explored in studies such as Jeong et al. (2012), Kiyono et al. (2016), Yoon (2017), and Mirzendehdel, Rankouhi, and Suresh (2018), which demonstrated the potential of safety-factor-based formulations for robust and failure-aware topology design.

While previous studies have proposed valuable strategies to extend stress-based topology optimization to non-ductile materials or to alternative failure theories, these developments have not yet been integrated within the BESO framework. In this context, the present work introduces an incremental yet relevant contribution by formulating and implementing a stress-based BESO method that combines alternative static failure criteria with a safety-factor-based formulation. Specifically, the methodology maximizes the global P-measure of the safety factor according to either the von Mises-Hencky or the Drucker-Prager failure criterion, enabling consistent topology optimization for materials with distinct yielding and failure behaviors.

The proposed formulation stabilizes the evolutionary process through sensitivity filtering and adaptive parameter control, ensuring consistent material redistribution during optimization. Through a set of representative numerical examples, the study demonstrates how different failure theories influence the resulting topologies, highlighting the method's capability to generate designs with reduced stress concentration and improved structural safety.

2 METHODOLOGY

2.1 Problem formulation

The P-norm base form can be adapted to approximate the minimum value of a set by employing a negative exponent. In this case, the influence of larger terms is progressively diminished as the exponent decreases. Following Kiyono et al. (2016), the P-measure is defined with an exponent $P \le -1$, so that maximizing this global measure applied to the elemental safety factor effectively increases the minimum safety factor within the structure.

The optimization problem can then be formulated as the maximization of the P-measure of a generic safety coefficient \bar{X} — associated with an arbitrary static failure theory — as:

Maximize
$$\{x\}$$
 $X_P^{\bar{X}}(\{x\})$

Subject to
$$\begin{cases} \{F\} - [K(\{x\})]\{U(\{x\})\} = \{\mathbf{0}\} \\ \sum_{e=1}^{nel} x_e V_e - V_{presc} = 0 \end{cases}$$
 (1)

With
$$\begin{cases} \{x\} = [x_1 \ x_2 \ ... \ x_{nel}]^T \\ x_e \in \{x_{min}, 1\} \end{cases} ,$$

where $\{x\}$ is the vector of pseudodensities, the design variables that define the material layout in the design domain. In the BESO framework, each element e is assigned either $x_e=1$ (solid) or $x_e=x_{min}$ (void), ensuring a discrete material distribution. The vectors $\{F\}$, $\{U\}$, and the matrix [K] correspond, respectively, to the global force vector, nodal displacement vector, and stiffness matrix of a linear-elastic finite element model. In addition, V_e denotes the volume of each element, V_{presc} the prescribed total volume, and nel the total number of finite elements.

As discussed, a safety-factor-based formulation is adopted in preference to equivalent stress measures for failure theories lacking a well-defined equivalent stress, such as brittle-material or pressure-sensitive criteria.

The global P-measure of the elemental safety factor \bar{X}_e is defined as:

$$X_{P}^{\bar{X}} = \left(\sum_{e=1}^{nel} \bar{X}_{e}^{P}\right)^{1/P} \mid P \le -1,$$
 (2)

with $\bar{X}_e \geq \varepsilon$, where ε is a small positive number to avoid numerical singularities.

The safety factor \bar{X}_e , derived from the failure locus, provides a consistent and generalizable metric across diverse failure theories.

2.2 Static failure evaluation

In structural design, static failure theories provide criteria to predict the onset of failure under a given stress state. They establish conditions under which a material undergoes either rupture or excessive distortion, corresponding respectively to fracture and yielding mechanisms. Mathematically, each theory is defined by a failure function \mathcal{F} , expressed in terms of the stress tensor \mathbf{T} and its invariants I_1 , I_2 , and I_3 , as follows:

$$\mathcal{F}(I_1, J_2, J_3) = 0, (3)$$

$$I_1 = \operatorname{tr}(\mathbf{T}),\tag{4}$$

$$\mathbf{S} \equiv \mathbf{T} - \frac{I_1}{3} \mathbf{I},\tag{5}$$

$$J_2 = \frac{1}{2}(\mathbf{S} : \mathbf{S}),\tag{6}$$

$$J_3 = \det(\mathbf{S}),\tag{7}$$

where tr(-) denotes the trace, (-):(-) the double-dot product, and det(-) the determinant operator. The function \mathcal{F} defines the failure (or yield) surface in the principal stress space, delimiting the stress combinations that do not cause failure (Dowling, 2013).

For each failure theory, it is often possible to define an equivalent stress measure $\overline{\sigma}$ and a critical stress σ_c , such that:

$$\overline{\sigma} \ge \sigma_c$$
 (failure), (8) $\overline{\sigma} < \sigma_c$ (safe).

Giraldo-Londoño and Paulino (2020) proposed a normalized formulation for a broad class of failure theories, defined as:

$$\mathcal{F}/\sigma_c = A(\theta)\sqrt{3J_2} + BI_1 + \Gamma I_1^2 - 1 = 0,\tag{9}$$

where A, B, and Γ are parameters specific to each theory and θ is the Lode angle.

A load multiplier ϱ can be introduced such that:

$$\varrho \mathbf{T} = \mathbf{T}_{c},$$
(10)

where \mathbf{T}_c represents the stress state at failure. The current stress state therefore deviates from the failure state by the factor ϱ . Substituting this scaling into the failure function yields:

$$\varrho A(\theta) \sqrt{3J_2} + \varrho BI_1 + \varrho^2 \Gamma I_1^2 - 1 = 0. \tag{11}$$

The safety factor \bar{X} is then defined as the smallest positive value of ϱ that satisfies Equation (11).

The associated stress index I is expressed as:

$$I \equiv 1/\bar{X}.\tag{12}$$

In practice, \bar{X} can be obtained directly from the analytical expression of the failure surface or, equivalently, from the evaluation of the failure function for each stress state. This formulation allows seamless integration of different static failure theories — such as von Mises-Hencky or Drucker-Prager — into the BESO framework through the computation of local safety factors and their global aggregation via the P-measure described previously.

2.3 Material interpolation

To implement the optimization problem, the material properties are interpolated according to the Solid Isotropic Material with Penalization (SIMP) scheme, which establishes a continuous relationship between the element pseudodensity x_e and its corresponding material property. Considering a homogeneous and isotropic material, the interpolated elastic modulus E_e is defined as:

$$E_e \equiv \chi_e^{\ q} E^0, \tag{13}$$

such that the constitutive matrix $[D_{\rho}]$ becomes:

$$[\mathbf{D}_e] \equiv x_e^{q} [\mathbf{D}^0], \tag{14}$$

where E^0 and $[D^0]$ denote, respectively, the elastic modulus and the constitutive matrix of the fully solid material.

In the SIMP interpolation, the penalization exponent q reduces the influence of intermediate pseudodensities, promoting a nearly binary material distribution. In the BESO method, although the final topology is strictly discrete, this exponent likewise smooths the contribution of elements in the sensitivity analysis, thereby stabilizing the evolution process and guiding the redistribution of material.

In the soft-kill implementation of the BESO method, solid and void elements are represented by pseudodensities $x_e = 1$ and $x_e = x_{min}$, respectively, with $x_{min} = 0.001$ adopted in this work to avoid numerical singularities.

For stress-based topology optimization, distinct penalization exponents are typically employed for the stiffness and stress interpolations, denoted by q and s, respectively. This distinction accounts for the nonlinear relationship between stiffness and stress with respect to the material density, allowing better control of stress concentrations and improving numerical stability during the optimization process, as employed in Xia et al. (2018) and Nabaki, Shen, and Huang (2019).

The corresponding interpolated quantities can be written as:

$$[\mathbf{k}_e] \equiv x_e^{\ q}[\mathbf{k}_e^0],\tag{15}$$

$$[K_{\rho}] = [L_{\rho}]^T [k_{\rho}] [L_{\rho}], \tag{16}$$

$$[\mathbf{D}_{\rho}^{s}] \equiv x_{\rho}^{s}[\mathbf{D}^{0}], \tag{17}$$

$$\{\boldsymbol{\sigma}_{e}\} \equiv [\boldsymbol{D}_{e}^{S}][\boldsymbol{B}_{e}]\{\boldsymbol{u}_{e}\},\tag{18}$$

where $[k_e^0]$ is the stiffness matrix of the solid element, $[k_e]$ the interpolated element stiffness matrix, $[L_e]$ the location matrix of the elemental degrees of freedom, $[K_e]$ the element stiffness matrix in the global coordinate system, $[D_e^s]$ the interpolated constitutive matrix for stress evaluation, $[B_e]$ the element strain-displacement matrix, $\{u_e\}$ the element nodal displacement vector, and $\{\sigma_e\}$ the corresponding element stress vector.

2.4 Sensitivity analysis

The sensitivity analysis is carried out using the adjoint method, which allows expressing the augmented objective function f in terms of the original objective function $X_P^{\bar{X}}$ and the constraint R, including the Lagrange multipliers $\{\Lambda_e^{\bar{X}}\}$ and λ^V :

$$R = \left\{ \Lambda_e^{\bar{X}} \right\}^T (\{F\} - [K]\{U\}) + \lambda^V \left(\sum_{e=1}^{nel} x_e V_e - V_{presc} \right), \tag{19}$$

$$f = X_P^{\bar{X}} + R. \tag{20}$$

For the sensitivity analysis, an effective stress measure was used according to Xia et al. (2018), leading to:

$$\frac{\partial \{\sigma_e\}}{\partial x_e} = [\mathbf{D}^0][\mathbf{B}_e] \frac{\partial \{u_e\}}{\partial x_e}.$$
 (21)

Through algebraic development, the sensitivity derivative becomes:

$$\frac{\partial f}{\partial x_e} = \left(\frac{\partial X_P^{\bar{X}}}{\partial \bar{X}_e} \left\{\frac{\partial \bar{X}_e}{\partial \{\sigma_e\}}\right\}^T [\boldsymbol{D}^0] [\boldsymbol{B}_e] [\boldsymbol{L}_e] - \left\{\boldsymbol{\Lambda}_e^{\bar{X}}\right\}^T [\boldsymbol{K}]\right) \frac{\partial \{\boldsymbol{U}\}}{\partial x_e} - \left\{\boldsymbol{\Lambda}_e^{\bar{X}}\right\}^T \frac{\partial [\boldsymbol{K}]}{\partial x_e} \{\boldsymbol{U}\} + \lambda^V V_e.$$
(22)

The term $\frac{\partial \{U\}}{\partial x_e}$ can be eliminated by defining the adjoint vector $\left\{ \pmb{\Lambda}_e^{ar{X}} \right\}$ such that:

$$\frac{\partial X_{P}^{\bar{X}}}{\partial \bar{X}_{e}} \left\{ \frac{\partial \bar{X}_{e}}{\partial \{\sigma_{e}\}} \right\}^{T} [\boldsymbol{D}^{0}] [\boldsymbol{B}_{e}] [\boldsymbol{L}_{e}] - \left\{ \boldsymbol{\Lambda}_{e}^{\bar{X}} \right\}^{T} [\boldsymbol{K}] \equiv [\boldsymbol{0}], \tag{23}$$

which leads to:

$$\frac{\partial f}{\partial x_e} = -\left\{ \Lambda_e^{\bar{X}} \right\}^T \frac{\partial [K]}{\partial x_e} \{ U \} + \lambda^V V_e, \tag{24}$$

$$[K]\{\Lambda_e^{\bar{X}}\} = \frac{\partial X_P^{\bar{X}}}{\partial \bar{X}_e} [L_e]^T [B_e]^T [D^0]^T \left\{ \frac{\partial \bar{X}_e}{\partial \{\sigma_e\}} \right\}. \tag{25}$$

Pseudo-forces are defined in the global and local systems as:

$$\left\{ \boldsymbol{F}_{e}^{\bar{X}} \right\} \equiv \frac{\partial X_{P}^{\bar{X}}}{\partial \bar{X}_{e}} [\boldsymbol{L}_{e}]^{T} [\boldsymbol{D}^{0}]^{T} \left\{ \frac{\partial \bar{X}_{e}}{\partial \left\{ \boldsymbol{\sigma}_{e} \right\}} \right\}, \tag{26}$$

$$\{\boldsymbol{f}_{e}^{\bar{X}}\} \equiv \frac{\partial X_{P}^{\bar{X}}}{\partial \bar{X}_{e}} [\boldsymbol{B}_{e}]^{T} [\boldsymbol{D}^{0}]^{T} \left\{ \frac{\partial \bar{X}_{e}}{\partial \{\boldsymbol{\sigma}_{e}\}} \right\}, \tag{27}$$

where the derivative of the P-measure can be obtained with:

$$\frac{\partial X_P^{\bar{X}}}{\partial \bar{X}_e} = (X_P^{\bar{X}})^{1-P} (\bar{X}_e)^{P-1}. \tag{28}$$

The characteristic adjoint system is given by:

$$[K]\{\Lambda^{\bar{X}}\} = \{F^{\bar{X}}\},\tag{29}$$

with $\{ \mathbf{F}^{\bar{X}} \}$ defined as:

$$\{\mathbf{F}^{\bar{X}}\} \equiv \sum_{e=1}^{nel} \{\mathbf{F}_e^{\bar{X}}\} \equiv \sum_{e=1}^{nel} [\mathbf{L}_e]^T \{\mathbf{f}_e^{\bar{X}}\}. \tag{30}$$

The variable $\{{\pmb \Lambda}^{ar X}\}$ can be recovered by defining $\{{\pmb \lambda}_e^{ar X}\}$ as in:

$$\sum_{e=1}^{nel} [\mathbf{L}_e]^T \{ \boldsymbol{\lambda}_e^{\bar{X}} \} \equiv \sum_{e=1}^{nel} \{ \boldsymbol{\Lambda}_e^{\bar{X}} \} \equiv \{ \boldsymbol{\Lambda}^{\bar{X}} \}. \tag{31}$$

The final sensitivity derivative can be expressed in the elemental domain with:

$$\frac{\partial f}{\partial x_e} = -\left\{\lambda_e^{\overline{X}}\right\}^T \frac{\partial [k_e]}{\partial x_e} \{u_e\} + \lambda^V V_e. \tag{32}$$

For a specific static failure theory, the derivative $\left\{\frac{\partial \bar{X}_e}{\partial \{\sigma_e\}}\right\}$ must be calculated, ensuring differentiability with respect to the stress components.

For the von Mises-Hencky or Distortion Energy (DE) criterion, the element safety factor is:

$$X_{DE_e} = \sqrt{2}\sigma_y \left[\left(\sigma_{xx_e} - \sigma_{yy_e} \right)^2 + \left(\sigma_{yy_e} - \sigma_{zz_e} \right)^2 + \left(\sigma_{zz_e} - \sigma_{xx_e} \right)^2 + 6 \left(\sigma_{xy_e}^2 + \sigma_{yz_e}^2 + \sigma_{zx_e}^2 \right) \right]^{-\frac{1}{2}}, \tag{33}$$

with derivative:

with derivative:
$$\left\{ \frac{\partial X_{DE_e}}{\partial \{\sigma_e\}} \right\} = \frac{X_{DE_e}^3}{2\sigma_y^2} \begin{cases} \sigma_{yy_e} - 2\sigma_{xx_e} + \sigma_{zz_e} \\ \sigma_{xx_e} - 2\sigma_{yy_e} + \sigma_{zz_e} \\ \sigma_{xx_e} + \sigma_{yy_e} - 2\sigma_{zz_e} \\ -6\sigma_{xy_e} \\ -6\sigma_{yz_e} \\ -6\sigma_{zx_e} \end{cases} ,$$
 (34)

where σ_{v} is the yield strength of the material.

For the Drucker-Prager criterion, the safety factor is approximated as:

$$X_{DP_e} \cong \left\{ \left[\frac{-2\sigma_{uc}\sigma_{ut}}{(\sigma_{ut} - \sigma_{uc})\sqrt{3J_{2e}} - (\sigma_{uc} + \sigma_{ut})I_{1e}} \right]^2 + \varepsilon \right\}^{1/2},\tag{35}$$

with $\sigma_{uc} < 0$ and σ_{ut} as the ultimate compressive and tensile strengths, respectively. The associated derivative was obtained via symbolic computational differentiation.

2.5 BESO iterative procedure

The BESO algorithm implemented in this work follows the soft-kill approach proposed by Huang and Xie (2010), originally designed for compliance minimization under a volume constraint, with modifications to address stress-based optimization and to improve robustness. The element removal/addition scheme is guided by sensitivity numbers $lpha_e^{ar{X}}$,

which quantify the effect of switching an element from solid to void or vice versa on the objective function. For the maximization-based problem addressed here, the sensitivity numbers are defined as:

$$\alpha_e^{\bar{X}} \equiv \frac{\partial f}{\partial x_e} - \lambda^V V_e,\tag{36}$$

where the subtraction of $\lambda^V V_e$ preserves the relative ordering of $\alpha_e^{ar{X}}$ in a regular mesh.

To enhance numerical stability and convergence, the sensitivity numbers are filtered, historically averaged, and normalized. Filtering at the nodal and elemental levels mitigates checkerboard patterns and mesh dependency, historical averaging smooths oscillations in the objective function, and min-max normalization (Zhou et al., 2021) ensures consistent comparison of sensitivities across elements.

The target volume for the next iteration, V_{k+1} , is calculated based on the evolutionary ratio ER:

$$V_{k+1} = \begin{cases} V_k(1 + ER) & V_k < V_{presc} \\ V_k(1 - ER) & V_k > V_{presc}, \\ V_k & V_k = V_{presc} \end{cases}$$

$$(37)$$

where k is the current iteration and V_k is the current volume.

With the target volume defined, the pseudodensity vector is updated based on the sorted sensitivity numbers: solid elements with $\alpha_e^{\bar{X}} \leq \alpha_{del}^{th}$ are removed, and void elements with $\alpha_e^{\bar{X}} > \alpha_{add}^{th}$ are added. Thresholds α_{del}^{th} and α_{add}^{th} are adaptively computed from V_{k+1} , the volume addition ratio AR, and its maximum AR_{max} , following the heuristic proposed by Huang and Xie (2010).

The iterative process continues until the prescribed volume is reached and the stopping criterion is satisfied. Convergence is assessed using the relative change of the objective function over the last 2N iterations:

$$crit_{k} \equiv \frac{\left|\sum_{i=1}^{N} X_{P \, k-i+1}^{\bar{X}} - \sum_{i=1}^{N} X_{P \, k-N-i+1}^{\bar{X}}\right|}{\sum_{i=1}^{N} X_{P \, k-i+1}^{\bar{X}}} \mid k \geq 2N, \tag{38}$$

where N=5 in this work. The evolution stops once $crit_k \le \tau$ with τ as a stopping criterion, ensuring that changes in the objective function become sufficiently small.

3 NUMERICAL RESULTS

Results are presented for two benchmark problems: the cantilever beam and the L-shaped profile. The cantilever beam was selected due to its evenly distributed tensile and compressive regions, which facilitate a clear visualization of differences among the applied failure theories. The L-shaped structure was chosen as a common benchmark in stress-based topology optimization studies, allowing assessment of the method's ability to reduce stress concentrations by eliminating the characteristic sharp corner.

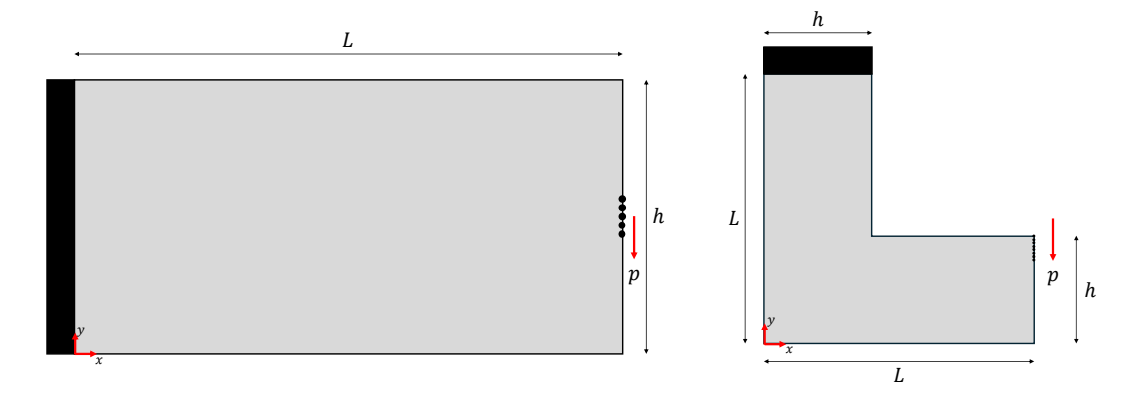


Figure 1 Initial topology and boundary conditions for cantilever beam (left) and L-shaped profile (right) examples.

3.1 Cantilever beam

The 2D cantilever beam example follows Nabaki, Shen, and Huang (2019). In the implemented approach, a distributed load was applied to five nodes (Figure 1), unlike the reference work, where the load was applied to the central node and six adjacent elements were excluded from both optimization and post-processing. This distributed loading reduces localized stress concentrations and avoids additional interference in the optimization problem.

Structural steel was first considered, consistent with the von Mises-Hencky static failure criterion. All parameters from the reference were adopted as in Table 1, except for the maximum volume addition ratio AR_{max} , the sensitivity filter radius r_{min} , and the P-norm exponent, which were not specified in the reference and were therefore set to values suitable for achieving comparable topologies. The results for topology and maximum von Mises equivalent stress are presented in Figure 2, showing good agreement with the reference work and highlighting differences compared to mean compliance minimization results.

Subsequently, the cantilever beam was analyzed as a gray cast iron structure, using material properties from Dowling (2013) and the Drucker-Prager criterion for static failure assessment. The verification employed the associated parameters from Table 1, and the resulting topology and stress distribution are shown in Figure 3.

Table 1 Parameters used for the cantilever beam example

Parameters	Quantity for specific failure theory (if applicable):
L - Beam length (mm)	200
h - Beam height (mm)	100
t - Beam width (mm)	1
p - Applied load (N)	-1500 (DE); -1000 (DP)
dx - Finite element length (mm)	1
dy - Finite element height (mm)	1
E - Young's modulus (MPa)	210000 (DE); 100000 (DP)
u - Poisson's ratio (-)	0.3
V_{presc} - Prescribed volume ratio (%)	{30, 40, 50}
ER - Evolutionary volume ratio (%)	2 (DE); 0.5 (DP)
AR_{max} - Maximum volume addition ratio (%)	4 (DE); 0.25 (DP)
r_{min} - Sensitivity filter radius (mm)	3
au - Stopping criterion tolerance (%)	0.01 (DE); {0.01, 0.1} (DP)
$\it q$ - Penalizing exponent for material interpolation (-)	3
s - Penalizing exponent for stress interpolation (-)	1
P - Penalizing exponent for P-measure (-)	-5 (DE); -4.5 (DP)
$\sigma_{\mathcal{Y}}$ - Yield strength (MPa)	358
$\sigma_{\!ut}$ - Tensile ultimate strength (MPa)	214
$\sigma_{\!uc}$ - Compressive ultimate strength (MPa)	-770

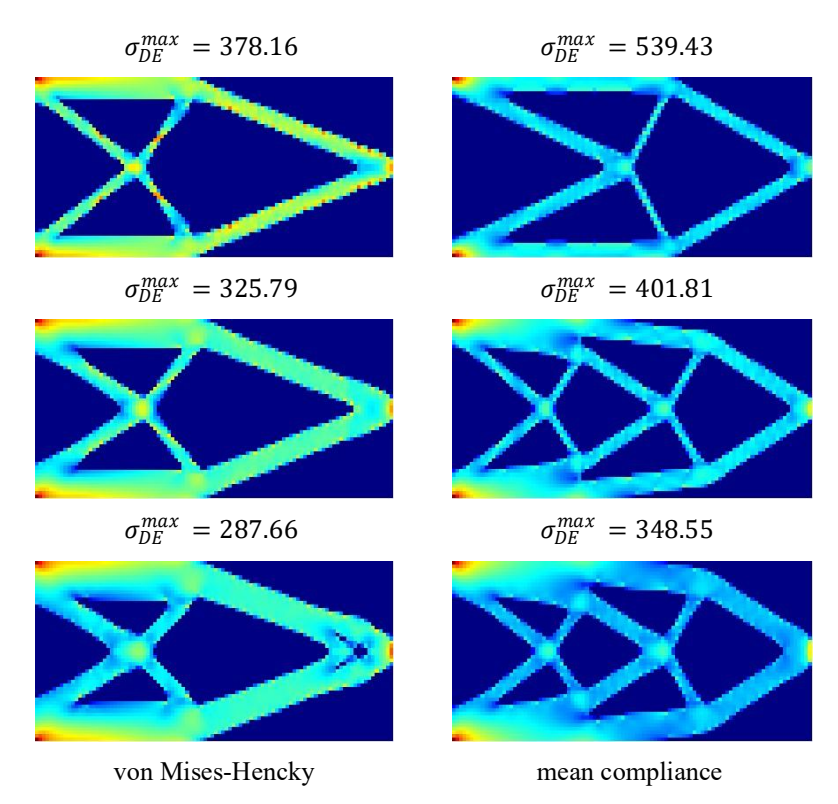


Figure 2 Cantilever beam results for P-measure maximization using the von Mises-Hencky theory and for mean compliance minimization; stress values in MPa; color map proportional to von Mises equivalent stress; prescribed volume ratios (from top to bottom) of 0.3, 0.4, and 0.5.

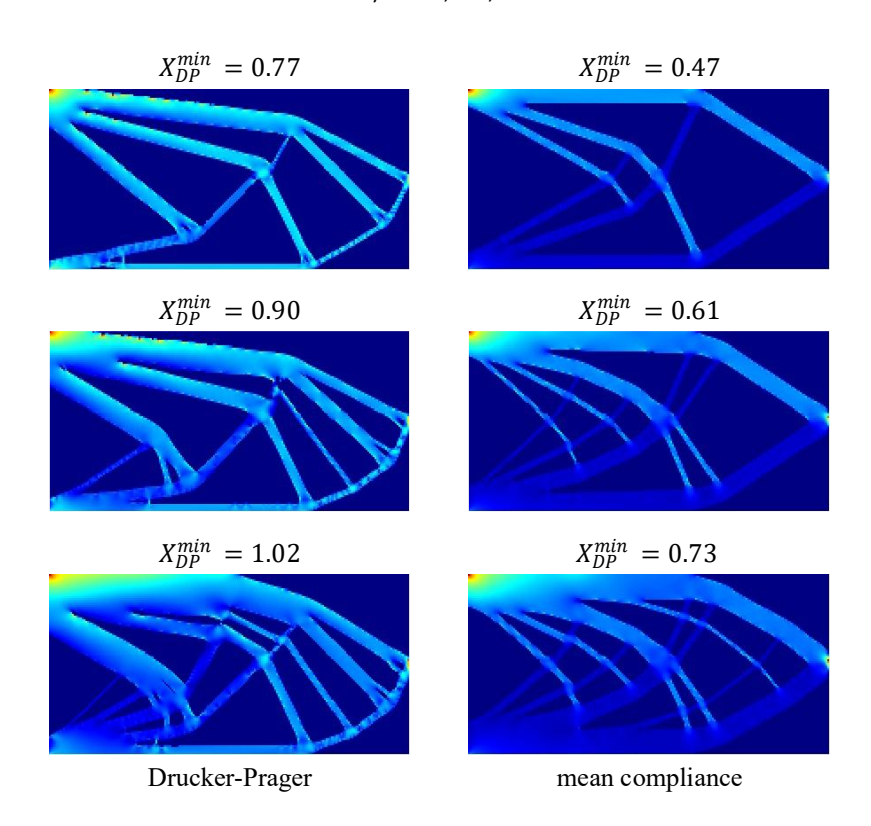


Figure 3 Cantilever beam results for P-measure maximization using the Drucker-Prager theory and for mean compliance minimization; color map proportional to the associated stress index; prescribed volume ratios (from top to bottom) of 0.3, 0.4, and 0.5.

3.2 L-shaped profile

The L-shaped profile example follows Xia et al. (2018), with dimensions, boundary conditions, and loading shown in Figure 1, and parameters listed in Table 2. Consistent with the reference, an artificial material and the von Mises-Hencky static failure theory were considered. All parameters from the reference were used, except for the filter radius. In Xia et al. (2018), the filter was applied both to the sensitivity numbers and to the pseudodensity vector. Despite this, their results retained the sharp corner of the L-shaped profile. To reduce the associated stress concentration, a filter radius of 1.5 mm was employed, producing the topology and stress distribution shown in Figure 4.

For the case of gray cast iron, with material properties from Dowling (2013), the Drucker-Prager criterion was applied for static failure analysis. The corresponding parameters from Table 2 were used, and the resulting topologies and stress distributions are presented in Figure 5.

Table 2 Parameters used	d for the L-s	haped profile	example.
--------------------------------	---------------	---------------	----------

Parameters	Quantity for specific failure theory (if applicable):
L - External length (mm)	200
h - Internal length (mm)	80
t - L-shaped width (mm)	1
p - Applied load (N)	-4 (DE); -500 (DP)
dx - Finite element length (mm)	1
dy - Finite element height (mm)	1
E - Young's modulus (MPa)	1 (DE); 100000 (DP)
u - Poisson's ratio (-)	0.3
V_{presc} - Prescribed volume ratio (%)	{30, 40, 50}
ER - Evolutionary volume ratio (%)	2 (DE); 1 (DP)
AR_{max} - Maximum volume addition ratio (%)	0.5
r_{min} - Sensitivity filter radius (mm)	1.5
au - Stopping criterion tolerance (%)	0.01
$\it q$ - Penalizing exponent for material interpolation (-)	3
s - Penalizing exponent for stress interpolation (-)	1
P - Penalizing exponent for P-measure (-)	-6 (DE); -4.7 (DP)
$\sigma_{\mathcal{Y}}$ - Yield strength (MPa)	1
$\sigma_{\!ut}$ - Tensile ultimate strength (MPa)	214
$\sigma_{\!uc}$ - Compressive ultimate strength (MPa)	-770

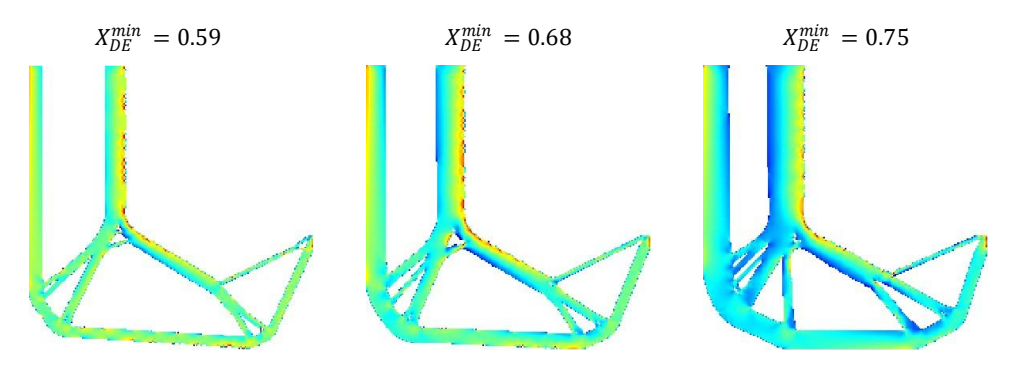


Figure 4 L-shaped profile: results for P-measure maximization using the von Mises-Hencky theory; color map proportional to the von Mises equivalent stress; prescribed volume ratios (left to right) of 0.3, 0.4, and 0.5.

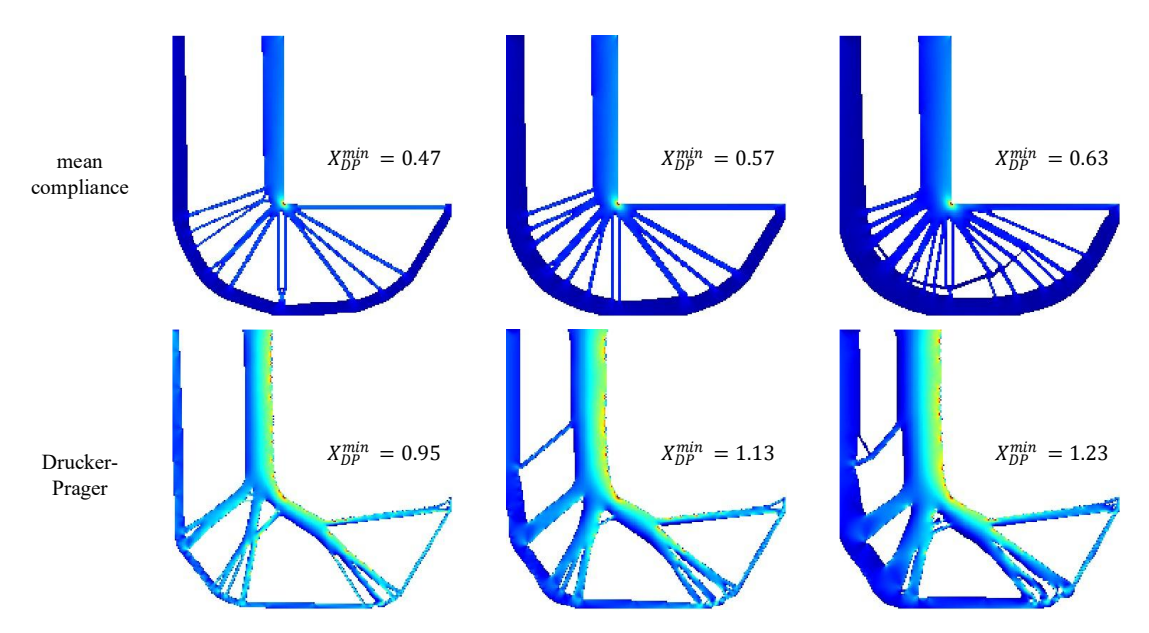


Figure 5 L-shaped profile: results for P-measure maximization using the Drucker-Prager theory and for mean compliance minimization; color map proportional to the associated stress index; prescribed volume ratios (left to right) of 0.3, 0.4, and 0.5.

4 CONCLUSION

For the cantilever beam, the implemented approach produced results consistent with Nabaki, Shen, and Huang (2019) in terms of topology and maximum von Mises equivalent stress, while differing considerably from the mean compliance minimization results (Figure 2).

Using the Drucker-Prager criterion, the methodology successfully generated topologies with higher safety factors compared to mean compliance minimization. For the same volume (Figure 3), the resulting structures were safer against static failure, reflecting the asymmetry between tensile and compressive strengths in materials compatible with the Drucker-Prager failure theory. With a downward vertical load, tensile stresses appear in the upper region and compressive stresses in the lower region; since the material is stronger in compression, more material is allocated to the tensile zone. The stress index visualization confirms this, with warmer colors indicating higher stress indexes in regions of lower safety factors.

For the L-shaped profile, topologies were consistent with Xia et al. (2018) regarding maximum von Mises equivalent stress. Differences in topologies arise from variations in problem formulation and, primarily, the filtering process. Using a smaller filter radius allowed for reduced stress concentrations by eliminating the sharp corner and enabled greater reorganization of elements, creating more structural members with different orientations (Figure 4).

Applying the Drucker-Prager criterion again resulted in topologies with higher safety factors than those obtained via mean compliance minimization. Material was preferentially allocated to the right vertical member, where tensile stresses dominate, at the expense of the more compressed left vertical member, as indicated by the stress index plot (Figure 5). This behavior was not observed with the von Mises-Hencky criterion, where symmetry in the yield limits resulted in more balanced member dimensions and stress distributions.

In both examples, some prescribed volumes produced topologies with minimum safety factors below 1. Since the optimization problem includes only a volume constraint and the global equilibrium condition, there is no explicit stress or safety factor constraint. Accordingly, achieving a safe design within the proposed methodology relies on selecting an appropriate prescribed volume and leveraging the safety factor through the objective function.

Author's Contributions: Conceptualization, Methodology, Writing – original draft, J. G. Lima Neto; Conceptualization, Writing – review & editing, Funding acquisition, Resources, Supervision, R. Pavanello.

Data Availability: Research data is only available upon request.

Editor: Eduardo Alberto Fancello and Paulo de Tarso Mendonça

References

Dowling, N. E. (2013). Mechanical Behavior of Materials: Engineering Methods for Deformation, Fracture, and Fatigue (4th ed.). Pearson.

Garcez, G. L. (2021). Stress-based structural topology optimization for design-dependent loads problems using the BESO method. Engineering Optimization, 55(2): 1–20.

Giraldo-Londoño, O.; Paulino, G. H. (2020). A unified approach for topology optimization with local stress constraints considering various failure criteria: von Mises, Drucker–Prager, Tresca, Mohr–Coulomb, Bresler–Pister, and Willam–Warnke. Proceedings of the Royal Society A, 476: 20200158.

Han, Y. (2024). Stress-based bi-directional evolutionary topology optimization for structures with multiple materials. Engineering with Computers, 40: 2905–2923.

Han, Y. S.; Xu, B.; Wang, Q.; Liu, Y. H.; Duan, Z. Y. (2021). Topology optimization of material nonlinear continuum structures under stress constraints. Computer Methods in Applied Mechanics and Engineering, 378: 113731.

Huang, X.; Xie, Y. M. (2007). Convergent and mesh-independent solutions for the bi-directional evolutionary structural optimization method. Finite Elements in Analysis and Design, 43: 1039–1049.

Huang, X.; Xie, Y. M. (2010). Evolutionary Topology Optimization of Continuum Structures: Methods and Applications. Wiley.

Jeong, S. H.; Park, S. H.; Choi, D. H.; Yoon, G. H. (2012). Topology optimization considering static failure theories for ductile and brittle materials. Computers & Structures, 110–111: 116–132.

Kiyono, C. Y.; Vatanabe, S. L.; Silva, E. C.; Reddy, J. N. (2016). A new multi-p-norm formulation approach for stress-based topology optimization design. Composite Structures, 140: 10–19.

Kundu, R. D.; Li, W.; Zhang, X. S. (2022). Multimaterial stress-constrained topology optimization with multiple distinct yield criteria. Extreme Mechanics Letters, 56: 101716.

Li, Y.; Chang, T.; Kong, W.; Wu, F.; Kong, X. (2024). Topological optimization of bi-directional progressive structures with dynamic stress constraints under aperiodic load. Applied Sciences, 14(1): 322.

Luo, Y.; Kang, Z. (2012). Topology optimization of continuum structures with Drucker–Prager yield stress constraints. Computers & Structures, 96–97: 65–75.

Ma, C.; Gao, Y.; Duan, Y.; Liu, Z. (2021). Stress relaxation and sensitivity weight for bi-directional evolutionary structural optimization to improve the computational efficiency and stabilization on stress-based topology optimization. Computer Modeling in Engineering & Sciences, 126(2): 715–738.

Mirzendehdel, A. M.; Rankouhi, B.; Suresh, K. (2018). Strength-based topology optimization for anisotropic parts. Additive Manufacturing, 23: 104–113.

Nabaki, K.; Shen, J.; Huang, X. (2019). Stress minimization of structures based on bidirectional evolutionary procedure. Journal of Structural Engineering, 145(9): 04019085.

Xia, L.; Zhang, L.; Xia, Q.; Shi, T. (2018). Stress-based topology optimization using bi-directional evolutionary structural optimization method. Computer Methods in Applied Mechanics and Engineering, 332: 356–370.

Xu, B.; Han, Y. S.; Zhao, L. (2020). Bi-directional evolutionary topology optimization of geometrically nonlinear continuum structures with stress constraints. Applied Mathematical Modelling, 80: 771–791.

Xu, B.; Han, Y. S.; Zhao, L. (2021). Bi-directional evolutionary stress-based topology optimization of material nonlinear structures. Structural and Multidisciplinary Optimization, 63(3): 1287–1305.

Yoon, G. H. (2017). Brittle and ductile failure constraints of stress-based topology optimization method for fluid–structure interactions. Computers & Mathematics with Applications, 73: 398–419.

Zhao, F.; Xia, L.; Lai, W. X.; Xia, Q.; Shi, T.-L. (2019). Evolutionary topology optimization of continuum structures with stress constraints. Structural and Multidisciplinary Optimization, 59(2): 647–658.

Zhou, E. L.; Wu, Y.; Lin, X. Y.; Li, Q. Q.; Xiang, Y. (2021). A normalization strategy for BESO-based structural optimization and its application to frequency response suppression. Acta Mechanica, 232: 1307–1327.